RSC Advances

PAPER

View Article Online
View Journal | View Issue

Cite this: *RSC Adv.*, 2022, **12**, 2820

Enhancement of triboelectricity based on fully organic composite films with a conducting polymer†

Moon Hyun Chung,[ab] Hyun-Jun Kim,[b] Seunghwan Yoo,[ab] Hakgeun Jeong*[b] and Kyung-Hwa Yoo*[a]

Received 6th October 2021
Accepted 1st December 2021

DOI: 10.1039/d1ra07408c

rsc.li/rsc-advances

Triboelectric nanogenerators (TENGs) based on ferroelectric organic materials have advantages of high flexibility, biocompatibility, controllable ferroelectric properties, *etc.* However, this has limited the electrical output performance due to their lower ferroelectric characteristics than those of inorganic ferroelectric materials. A lot of effort has been made to improve the organic ferroelectric characteristics through composites, surface modifications, structures, *etc.* Herein, we report TENGs made of ferroelectric composite materials consisting of poly(vinylidene fluoride-*co*-trifluoroethylene) (PVDF-TrFE) and poly(3,4-ethylenedioxythiophene):poly(styrenesulfonate) (PEDOT:PSS). The composite was prepared by simply blending PVDF-TrFE and PEDOT:PSS with a weight ratio from 0% to 60%. When the ratio was 20%, the ferroelectric-crystalline phase was enhanced and the highest dielectric constant was observed. Accordingly, the TENGs consisting of 20% composite film and polyimide exhibited the best output performance: the maximum open circuit voltage and short circuit current were ~15 V and ~2.3 μA at 1 Hz oscillation, respectively. These results indicate that the ferroelectric characteristics of PVDF-TrFE can be enhanced by adding PEDOT:PSS as a nanofiller.

1 Introduction

Triboelectric nanogenerators (TENGs) based on ferroelectric polymers, self-powered energy harvesters, have attracted considerable attention because they can convert low-frequency and irregular mechanical energy to electrical energy. Also, they can be flexible, light-weight, bio-compatible, low-temperature, and solution-processable.[1–3] They provide opportunities for application to self-powered electronics, such as the Internet-of-Things, sensors, and wearable and healthcare devices.[4–7] TENGs have many harvesting applications, such as mechanical, thermal, magnetic, and solar.[8,9] Specifically, a flutter-driven TENG (FTENG) can use small-scale wind energy by utilizing a fluctuating object in the air flow, and it directly converts it to electric energy based on triboelectrification and electrostatic induction.[10,11] Moreover, the electrical output performance of TENGs is affected by the ferroelectric characteristics and surface charges. Thus, TENGs of ferroelectric polymer materials afford an improvement through the use of various methods, such as composite materials, structure, relative permittivity, and surface modifications.[12,13]

Among ferroelectric polymer materials, such as polyvinylidene fluoride (PVDF) and its copolymers, are extensively used for TENGs and piezoelectric nanogenerator active films because of their outstanding chemical resistivity, flexibility, biocompatibility, and mechanical and controllable ferroelectric properties.[14,15] PVDF has five phases, including α, β, γ, δ, and ε. In particular, the β and γ phases can affect the ferroelectric characteristics and promote the surface charge density. Thus, that phases need to be improved.[16,17] The electrical output performance of PVDF is limited owing to its low-ferroelectric properties,[18] and PVDF is used to enhance the ferroelectric properties by using its copolymer. Among the copolymers, poly(vinylidene fluoride-*co*-trifluoroethylene) (PVDF-TrFE), the ferroelectric properties and dielectric are higher than those of PVDF and the others owing to the TrFE monomers.[19,20] Thus, they are good candidates as host materials for TENGs.

When it comes to a contact-separation operational mode in TENGs, it can lead to deformation and can cause the wear of the surface during energy harvesting. This can lead to a negative influence on the electrical output performance. The additive materials with nanoscale dimensions adding to the host material that called nanofillers. Through the adequate nanofillers added to the host materials, it can be enhanced physical properties of the host materials. Moreover, this approach involves modifying the bulk properties of materials based on

[a]*Department of Physics, Yonsei University, 50 Yonsei-ro, Seodaemun-gu, Seoul 03722, Republic of Korea. E-mail: khyoo@yonsei.ac.kr*

[b]*Energy ICT Convergence Research Department, Energy Efficiency Research Division, Korea Institute of Energy Research, 152 Gajeong-ro, Yuseong-gu, Daejeon 34129, Republic of Korea. E-mail: hgjeong@kier.re.kr*

† Electronic supplementary information (ESI) available. See DOI: 10.1039/d1ra07408c

the functionalization of the chemical structure.[21,22] Therefore, ferroelectric materials with nanofillers can increase the physical properties and the relative dielectric constant, which plays a significant role in the generation of triboelectric charges.[23,24] Inorganics, metal oxide nanoparticles, and conducting materials such as $BaTiO_3$,[18] Au,[23] AlO_x,[25] Ag,[26] carbon nanotubes,[27] polyaniline,[28] and so on,[29,30] have been utilized as nanofillers in the ferroelectric polymers to enhance their electrical output.

Among the conducting polymers, poly(3,4-ethylenedioxythiophene)–poly(styrenesulfonate) (PEDOT:PSS) has the advantages of a flexible, highly stable, and low-intrinsic thermal conductivity, and can be used in a solution process.[31,32] Additionally, it has a higher electrical conductivity than other conducting polymers.[33] Hence, PEDOT:PSS has been extensively used for the top and bottom electrodes of devices, buffer layer of optoelectronic devices, and as thermoelectric materials because of the aforementioned properties.[34–38] There are some studies has been conducted to fabricate the PEDOT:PSS coated on PVDF-TrFE films, but the characteristics of the composite films have yet to researched.[39] We expect that TENG composite films that PEDOT:PSS serves as a nanofiller in PVDF-TrFE.

In this study, we fabricated fully organic materials for TENG films and proposed PEDOT:PSS as a nanofiller in PVDF-TrFE composite films to increase the electrical output performance of the films. Using X-ray diffraction (XRD), Fourier transform infrared (FT-IR), and differential scanning calorimetry (DSC) characterization, we investigated the effect of PEDOT:PSS at different concentrations on PVDF-TrFE composite films, in terms of the ferroelectric crystallization of the phase. We then optimized the PVDF-TrFE/PEDOT:PSS composite by varying the PEDOT:PSS concentration. The electrical output enhancement of the TENG films with PVDF-TrFE/PEDOT:PSS composite films was then measured. The dielectric constants of the PVDF-TrFE films and PVDF-TrFE/PEDOT:PSS composite films were evaluated. Furthermore, we demonstrated an FTENG using PVDF-TrFE/PEDOT:PSS composite films in the presence of air flow.

2 Experimental section

2.1 Materials

PEDOT:PSS (Clevios PH1000) solution was purchased from Heraeus (Germany). PVDF-TrFE (70–30 mol%) copolymer powder and DMF were purchased from Piezotech (France) and Sigma-Aldrich (USA), respectively. A polyethylene terephthalate (PET)/indium tin oxide (ITO) film (125 μm, 60 Ω sq^{-1}) and conductive copper foil tape (Cu tape, thickness = 80 μm) were obtained from Sigma-Aldrich and 3M (USA), respectively. Polyimide tape (PI tape, thickness = 60 μm) was purchased from DupontTM (USA).

2.2 Preparation of the PVDF-TrFE/PEDOT:PSS composite films

PVDF-TrFE/PEDOT:PSS composite films were prepared as shown in Fig. S1.† First, the PEDOT:PSS solution in water was dispersed in DMF (10 mL) solvent at a certain fraction (0–60 wt% based on its PVDF-TrFE weight), and PVDF-TrFE copolymer powder (2.5 g) was added to the PEDOT:PSS/DMF solution, followed by stirring at 35 °C for 12 h (Fig. S1a†). To fabricate the PVDF-TrFE/PEDOT:PSS composite films (Fig. S1b†), the composite solution was poured into the silicon

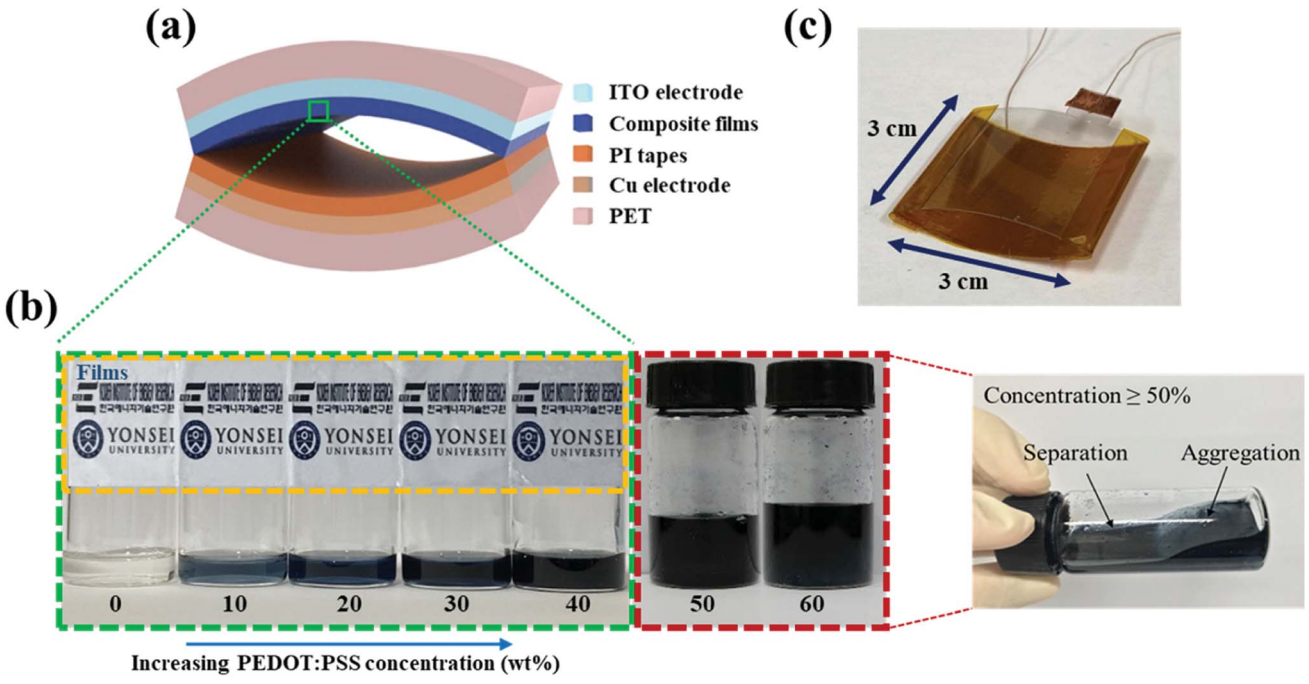

Fig. 1 (a) Schematic structure of PVDF-TrFE/PEDOT:PSS composite films based TENG. (b) Optical images demonstrating the solutions after blending the PVDF-TrFE with increasing PEDOT:PSS concentration (0% to 60%) from left to right. The insets (yellow dot square) show the PVDF-TrFE and the PVDF-TrFE/PEDOT:PSS composite films. (c) Photo of TENG with PVDF-TrFE/PEDOT:PSS composite films.

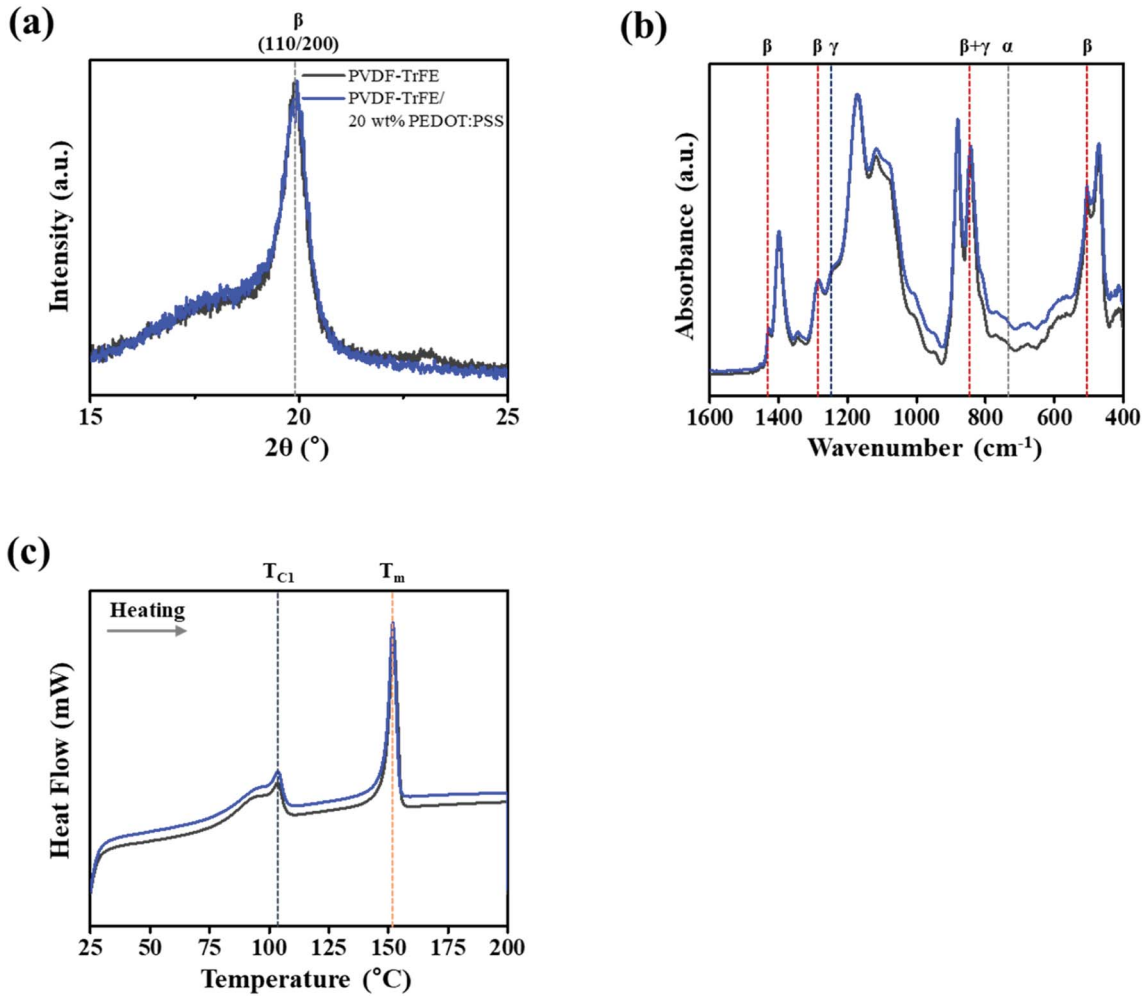

Fig. 2 The PVDF-TrFE/PEDOT:PSS composite films with different PEDOT:PSS contents of 0% and 20%: (a) XRD analysis, (b) FT-IR spectra from 400 cm^{-1} to 1600 cm^{-1}, and (c) DSC scan results heat flow *vs.* temperature during heating.

square mold with a size of 40 × 40 × 0.1 mm^3 (inner 30 × 30 × 0.1 mm^3) (width (W) × depth (D) × height (H)) on the PET/ITO, and flattened with a blade. The silicone mold was then peeled off, followed by annealing in a vacuum chamber at 30 °C for 1 h and then at 80 °C for 3 h. Finally, the PET/ITO film that was not covered with the composite film was removed except for the part where the copper wire was connected. The thickness of the composite film measured by using a surface profiler (DektakXT stylus profiler, Bruker, USA) was ~17 μm.

2.3 Fabrication of triboelectric nanogenerator

An arch-shaped TENG was fabricated by bending composite film/ITO/PET and PET/Cu tape/PI layers of the same size (contact area: 30 × 30 mm^2), and was then sealed at the two short edges with PI tape. Thus, the composite films of PVDF-TrFE/PEDOT:PSS and PI were face to face (Fig. 1a and c). Subsequently, the two electrodes were connected using copper wires.

Table 1 Relative fraction of the electroactive phase (F_{EA}) and the degree of ferroelectric crystallinity (X_C) of the poly(vinylidene fluoride-*co*-trifluoroethyle)/poly(3,4-ethylenedioxythiophene):poly(styrenesulfonate) (PVDF-TrFE/PEDOT:PSS) composite films at various PEDOT:PSS concentrations from 0% to 40% based on Fourier transform infrared spectroscopy and differential scanning calorimetry, respectively

	PVDF-TrFE	10 wt% PEDOT:PSS	20 wt% PEDOT:PSS	30 wt% PEDOT:PSS	40 wt% PEDOT:PSS
F_{EA} (%)	76.46	73.32	70.72	66.86	62.66
X_C (%)	30.10	30.82	37.11	29.08	31.30

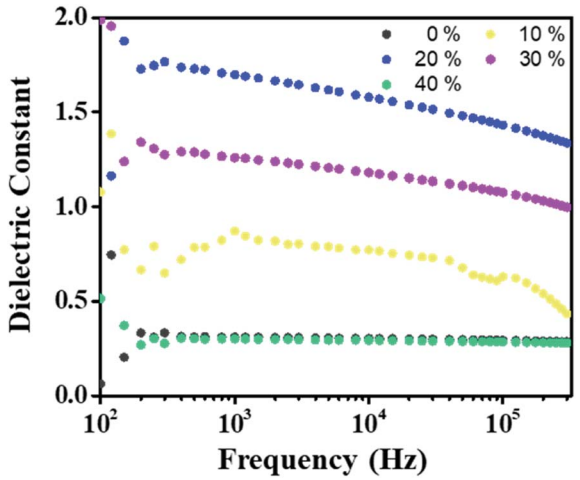

Fig. 3 Comparison of the dielectric constant for the PVDF-TrFE/PEDOT:PSS composite films with different PEDOT:PSS concentration from 0% to 40% at 300 K.

2.4 Fabrication of FTENG

The FTENG was composed of PVDF-TrFE/PEDOT:PSS composite films, a Cu tape electrode, PI films, and polycarbonate (PC). A PC cuboid with inner dimensions of 30 mm × 75 × 30 mm^3 (width (W) × depth (D) × height (H)) was made using a laser cutter. PVDF-TrFE/PEDOT:PSS composite films were coated on Cu tape, as described in Section 2.2. A piece of PVDF-TrFE/PEDOT:PSS composite film/Cu tape (30 × 75 mm^2) was attached to the PC plates at the top and bottom. Two electrodes were connected using copper wires. The PI film (30 × 75 mm^2, 65 μm) was fixed at one end on a bluff body.

2.5 Characterization

The surface morphology was confirmed using field emission scanning electron microscope (FE-SEM, JSM-6500F, JEOL, Japan). The structures of the composite films were investigated using XRD (D/max-2500 pc, Rigaku, Japan), FT-IR spectroscopy (Nicolet iS50, Thermo Fisher Scientific Instrument, USA), and DSC (DSC 4000, PerkinElmer, USA). The output performance of the TENG was measured using an oscilloscope (DPO 2002 B, Tektronix, USA), a low-noise current preamplifier (Model SR 570, Stanford Research Systems, Inc., USA), and an electrometer (6517 B, Keithley, USA). A function generator and mechanical wave driver (PI-8127 and SF-9324, PASCO, USA) were used to provide mechanical motion for the TENG. The capacitance of the composite films was measured using an LCR meter (E4980AL capacitance meter, Keysight, USA) in the frequency range of 100 Hz to 300 MHz. The airflow rate was estimated using a hot-wire anemometer (Testo 425, Testo SE & Co. KGaA, Germany).

3 Results and discussions

We prepared PVDF-TrFE/PEDOT:PSS composite films with weight ratios in the range of 0–40%. PVDF-TrFE is insoluble in water, and PEDOT:PSS is a water-based solution; thus, when PEDOT:PSS is added at a weight ratio greater than 40%, the solution is aggregated. However, the composite solution with a ratio smaller than 40% was well dispersed, and the film made from the composite solution was semi-transparent (Fig. 1b). The morphology of PVDF-TrFE/PEDOT:PSS composite films was analyzed by FE-SEM as shown in Fig. S2.† It consisted of the surface of rod-like shape. To investigate the effect of PEDOT:PSS on the crystalline phase of PVDF-TrFE, we measured the XRD spectra of the composite films in the 2θ range of 15–25° (Fig. 2a and S3a†). All films yielded a peak at 19.8°, which is associated with the β-phase at the (110) and (200) planes.[40,41] These results indicate that the crystallinity of PVDF-TrFE did not significantly affect by adding PEDOT:PSS.

Using FT-IR spectroscopy, we investigated the films for the transformation of phases and chain orientation within a wavenumber range of 400–1600 cm^{-1}. The spectra reveal important information about PVDF-TrFE and PVDF-TrFE/PEDOT:PSS composite films on the basis of the presence of the crystalline phase (Fig. 2b and S3b†). Crystallization of the β + γ phase was observed in all the films in the absorption bands at 840 cm^{-1}.[42] The strong peak was classified as a characteristic of the β + γ phase, which is a characteristic of CF_2 symmetric stretching. In addition, the peaks at 1430 and 1288 cm^{-1} is attributed to the β phase. The presence of the γ phase was observed at 1235 cm^{-1}. The bands at 763 cm^{-1} were associated with the α-phase.[43,44]

Evaluation of the electroactive phase (β + γ phase) fraction (F_{EA}) in the samples was calculated using the Lambert–Beer law eqn (1):[45]

$$F_{EA}\ (\%) = \frac{I_{EA}}{\left(\frac{K_{EA}}{K_{\alpha}}\right) I_{\alpha} + I_{EA}} \times 100 \quad (1)$$

Herein, I_α and I_{EA} are the absorbance intensities of the FT-IR peak at 763 cm^{-1} (α phase) and 840 cm^{-1} (β + γ phase), respectively. K_α and K_{EA} are the absorption coefficients at 763 cm^{-1} and 840 cm^{-1}, respectively; $K_\alpha = 6.1 \times 10^4$ cm^2 mol^{-1}, $K_{EA} = 7.7 \times 10^4$ cm^2 mol^{-1}.[44,46] The calculation indicates that the F_{EA} values decreased up to 62.66% with higher PEDOT:PSS

Table 2 Thickness and the dielectric constant values of the PVDF-TrFE/PEDOT:PSS composite films at various PEDOT:PSS concentrations from 0% to 40%

	PVDF-TrFE	10 wt% PEDOT:PSS	20 wt% PEDOT:PSS	30 wt% PEDOT:PSS	40 wt% PEDOT:PSS
Thickness (μm)	17.95	17.03	16.94	16.65	16.69
Dielectric constant (at 1 kHz)	0.31	0.87	1.70	1.25	0.30

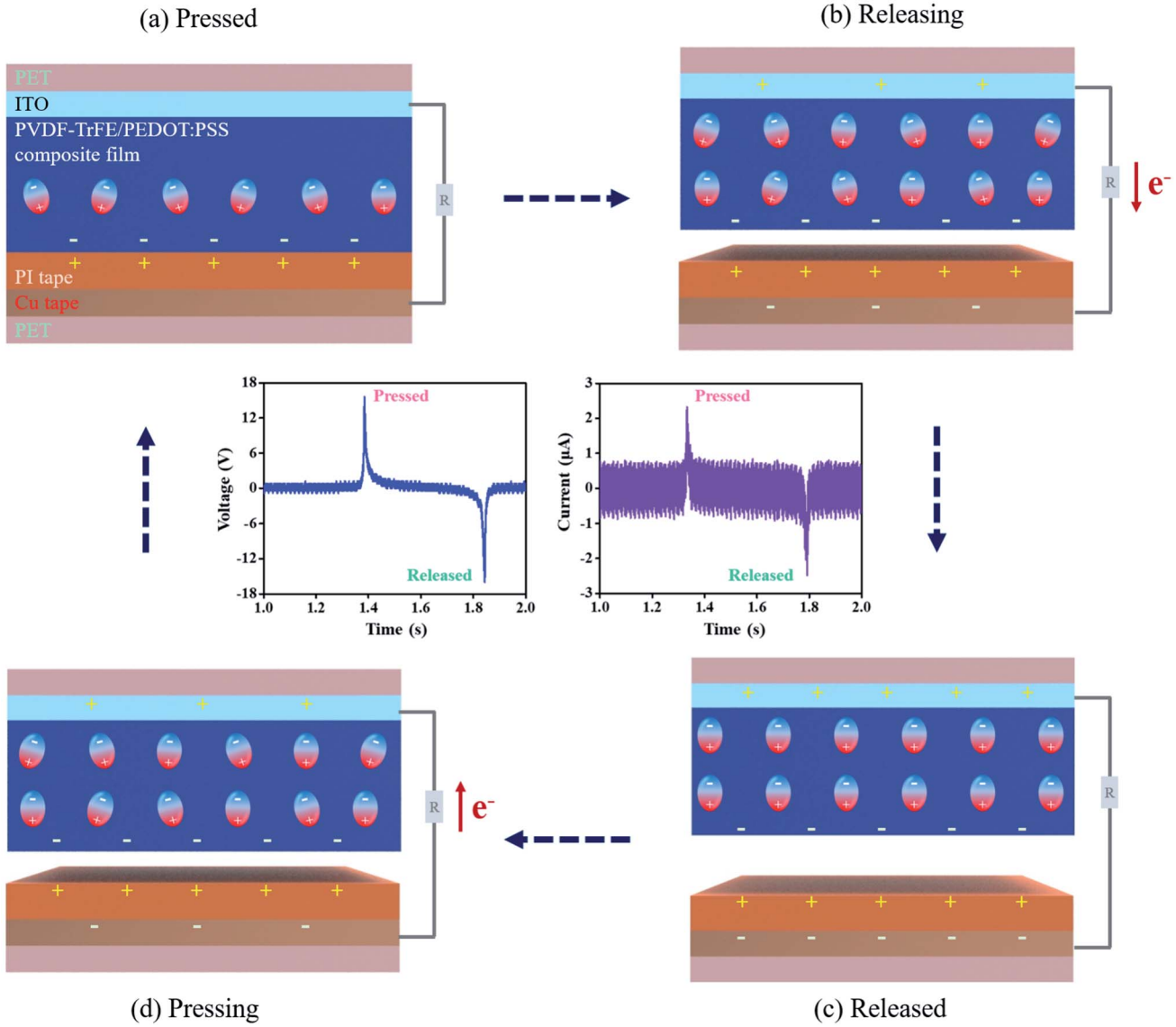

Fig. 4 Working mechanism of TENG with the PVDF-TrFE/PEDOT:PSS composite films: (a) pressed, (b) releasing, (c) released and (d) presssing.

content (Table 1). The α-phase of the PVDF-TrFE/PEDOT:PSS composite films increased at 763 cm^{-1} because the C–S–C peak of PEDOT:PSS appears at approximately 761 cm^{-1} (Fig. S3c†).[47] The F_{EA} values could be reduced by increasing the PEDOT:PSS concentration. To confirm the ferroelectric crystallinity of PVDF-TrFE/PEDOT:PSS composite films, DSC was conducted for thermal analysis between 25 °C and 200 °C at a heating rate of 10 °C min^{-1}. Fig. 2c and S3d† shows the DSC results. The two peaks in the endothermic heat flow curves during heating were identified, wherein the first peak (T_{c1}) corresponded to the ferroelectric to paraelectric transition and the second peak represented the melting transition (T_m).[48,49] The crystallinity (X_c) of PVDF-TrFE/PEDOT:PSS (0% to 40%) composite films was calculated on the basis of DSC scans, according to eqn (2).[50] Respective values are listed in Table 1.

$$X_c\ (\%) = \frac{\Delta H_m}{\Delta H_m^0} \times 100 \quad (2)$$

where ΔH_m is the melting enthalpy from the area of T_m peak and ΔH_0 is the enthalpy of the 100% crystalline PVDF-TrFE (91.45 J g^{-1}) that was obtained from the literature.[51] Increasing the PEDOT:PSS concentration in the films by 20 wt%, the X_c was observed to increase 37.11%. At 30% and 40% PEDOT:PSS concentration, the X_c reduced to the similar value to that of PVDF-TrFE. It seems that excessive PEDOT:PSS disturbs the form of ferroelectric crystallinity. These DSC results indicate that PEDOT:PSS is an effective filler used to improve the ferroelectric characteristics. Additionally, this demonstrated that the PVDF-TrFE doped with 20 wt% PEDOT:PSS reached the highest ferroelectric phase. In addition, to investigate the dielectric characteristics, we tested the capacitance of the PVDF-TrFE films and PVDF-TrFE/PEDOT:PSS composite

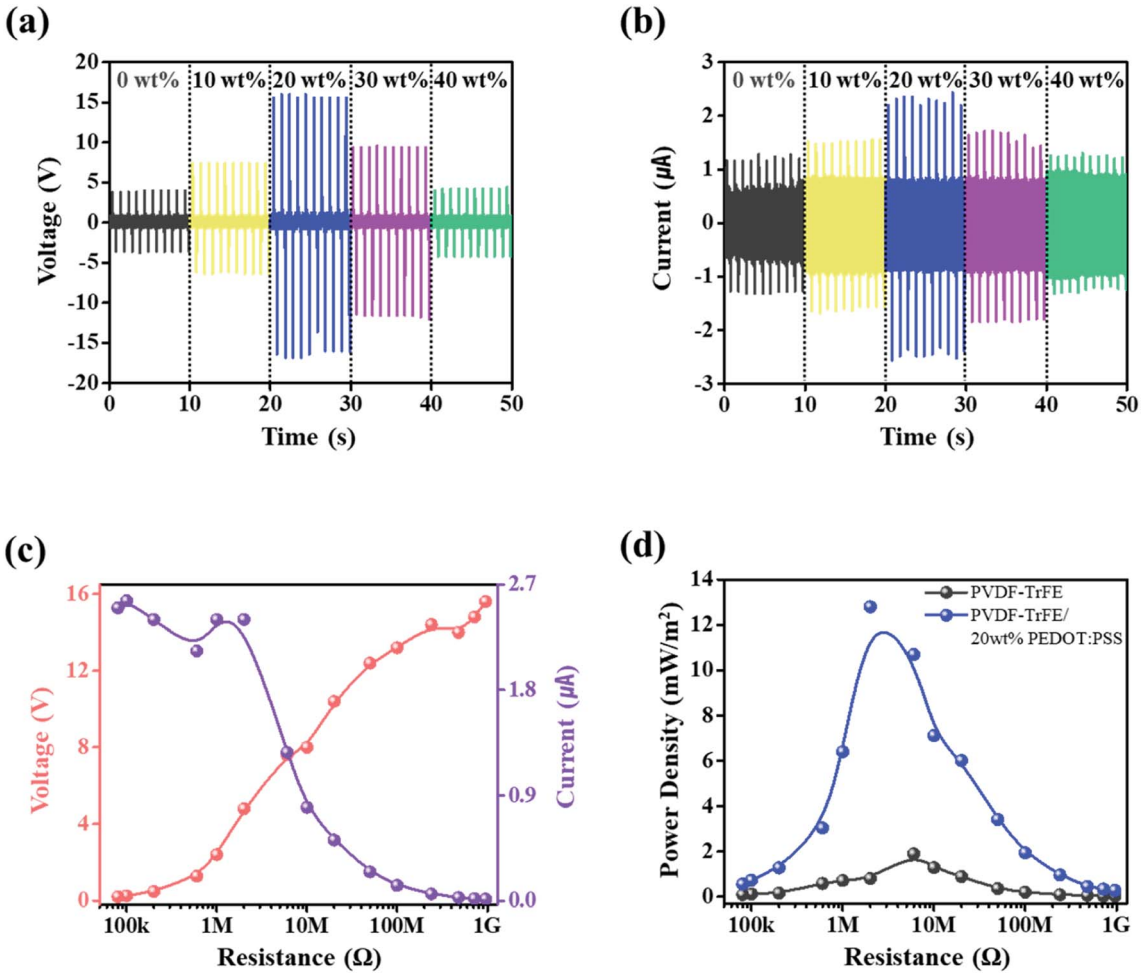

Fig. 5 Generated electrical output performance of TENG with the PVDF-TrFE/PEDOT:PSS composite at various PEDOT:PSS concentrations from 0% to 40%: Measured (a) open-circuit voltage and (b) closed-circuit current. (c) Output voltage and current of the PVDF-TrFE/20 wt% PEDOT:PSS composite films with the external load resistance varying from 80 kΩ to 960 MΩ. (d) Calculated the power density with at difference external load resistances of the PVDF-TrFE films and the PVDF-TrFE/20 wt% PEDOT:PSS composite films.

films. It was measured at 300 K in the frequency range of 100 Hz to 300 MHz, and the dielectric constant was transformed, as shown in Fig. 3. The dielectric constant (ε_r) was defined according to eqn (3),[52]

$$\varepsilon_r = \frac{C \times d}{\varepsilon_0 \times A} \quad (3)$$

where C is the capacitance, d is the thickness of the films (Table 2), ε_0 is the permittivity of air (8.85×10^{-12} F m^{-1}), and A is the active area of the films (0.0009 m^2). The results show that the dielectric constant value increases for contents up to 20 wt% PEDOT:PSS. In fact, the PVDF-TrFE/20 wt% PEDOT:PSS composite films yielded a higher dielectric constant (1.70 at 1 kHz) compared with those of PVDF-TrFE films (0.31 at 1 kHz) (Table 2). For contents higher than 20 wt% PEDOT:PSS, the dielectric constant decreased, which seems to be attributed to the decrease in the ferroelectric crystallinity and the electrical nature of PEDOT:PSS. We expect that this is because of the formation of microcapacitors in the nanocomposite because of the presence of nanofillers.[21] Consequently, the ferroelectric characteristics of the composite films improved and it has the capability to enhance the triboelectric charges accumulate.[23]

The working mechanism of the fabricated TENG, which includes triboelectrification and electrostatic induction, is shown in Fig. 4. As shown in Fig. 4a, when the composite films and the PI tapes are in contact, the opposite charges are equally generated between the composite and PI tapes of the contact surfaces. The composite films generated more electrically negative charges than the PI tapes.[53,54] Releasing the two films, the potential difference drives electrons from the ITO electrode to the Cu electrode (Fig. 4b)The electron flows continually until the maximum value of V_o is reached as the composite films fully separate from the original states (Fig. 4c). In sequence, the electrons are driven from the Cu electrode back to the ITO electrode, decreasing the amount of induced charges when the composite films approach the PI tapes (Fig. 4d). Consequently, an alternating current is generated by the contact and separation modes between the composite films and PI tapes.

To assess the electrical output performance of the PVDF-TrFE and PVDF-TrFE/PEDOT:PSS composite films, a wave

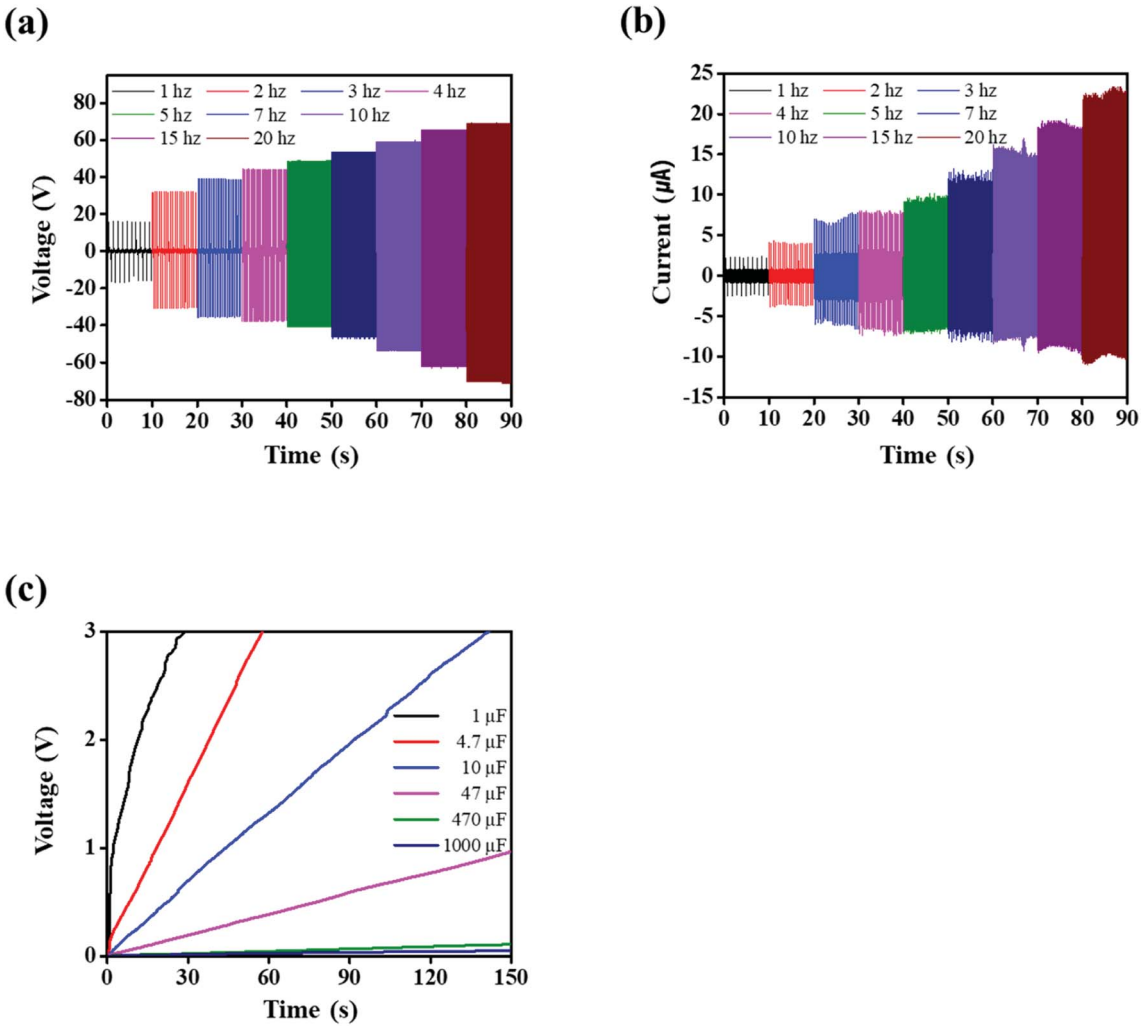

Fig. 6 PVDF-TrFE/20 wt% PEDOT:PSS composite films at different oscillations from 1 Hz to 20 Hz: (a) voltage and (b) current. (c) Charging profiles of capacitors at an oscillation of 20 Hz.

driver was used for the periodic contact and separation modes. The applied tapping force was ~8 N with 1 Hz oscillation, and the maximum distance of the contact separation was set to 7 mm. Fig. 5a and b shows the open-circuit voltage and closed-circuit current of PVDF-TrFE and PVDF-TrFE/PEDOT:PSS composite piezoelectric films containing different concentrations of PEDOT:PSS. PVDF-TrFE films generated an open-circuit voltage (V_o) equal to 4 V and a short-circuit current (I_{sc}) equal to 1.16 μA. As the concentration of PEDOT:PSS increased, V_o and I_{sc} were observed to increase up to 20 wt% PEDOT:PSS to respective values equal to 15.6 V and 2.32 μA, respectively. For PEDOT:PSS contents above 20 wt%, V_o and I_{sc} decreased. It seems that the predominance of PEDOT:PSS can be attributed to the reduced ferroelectric characteristics. These trends appear similar to the results of the preceding analysis.

The TENG can be explained by an inherent capacitive behavior, and we expected the quantities of triboelectric charges with electrical potential according to eqn (4):[55,56]

$$Q = C \times V_{\text{Tribo}} = \varepsilon_0 \varepsilon_r \frac{A \times V_{\text{Tribo}}}{d} \quad (4)$$

where Q is the surface charge, C is the capacitance, and V_{Tribo} is the triboelectric voltage. Q depends on V_{Tribo}, and the dielectric constant is defined in accordance with eqn (4). Herein, the values of V_{Tribo} changed with the concentration of PEDOT:PSS; as a result, the surface charge also changed. In addition, we calculated the triboelectric charge density with the relationship Q, V_{Tribo}, and dielectric constant by using eqn (5):[57]

$$\sigma = \frac{V_{\text{Tribo}} \varepsilon_0 \varepsilon_r}{d} \quad (5)$$

where σ is the surface charge density. The calculated values of σ for all samples were 0.52, 6.05, 13.90, 6.25, and 0.67 μC m^{-2} for PVDF-TrFE/PEDOT:PSS composite films at the concentrations of 0% to 40%, respectively. As a result, this shows the same tendency as those of the experimental and calculated results. We predict that PEDOT:PSS enhances the surface charge density by improving the ferroelectric characteristics.

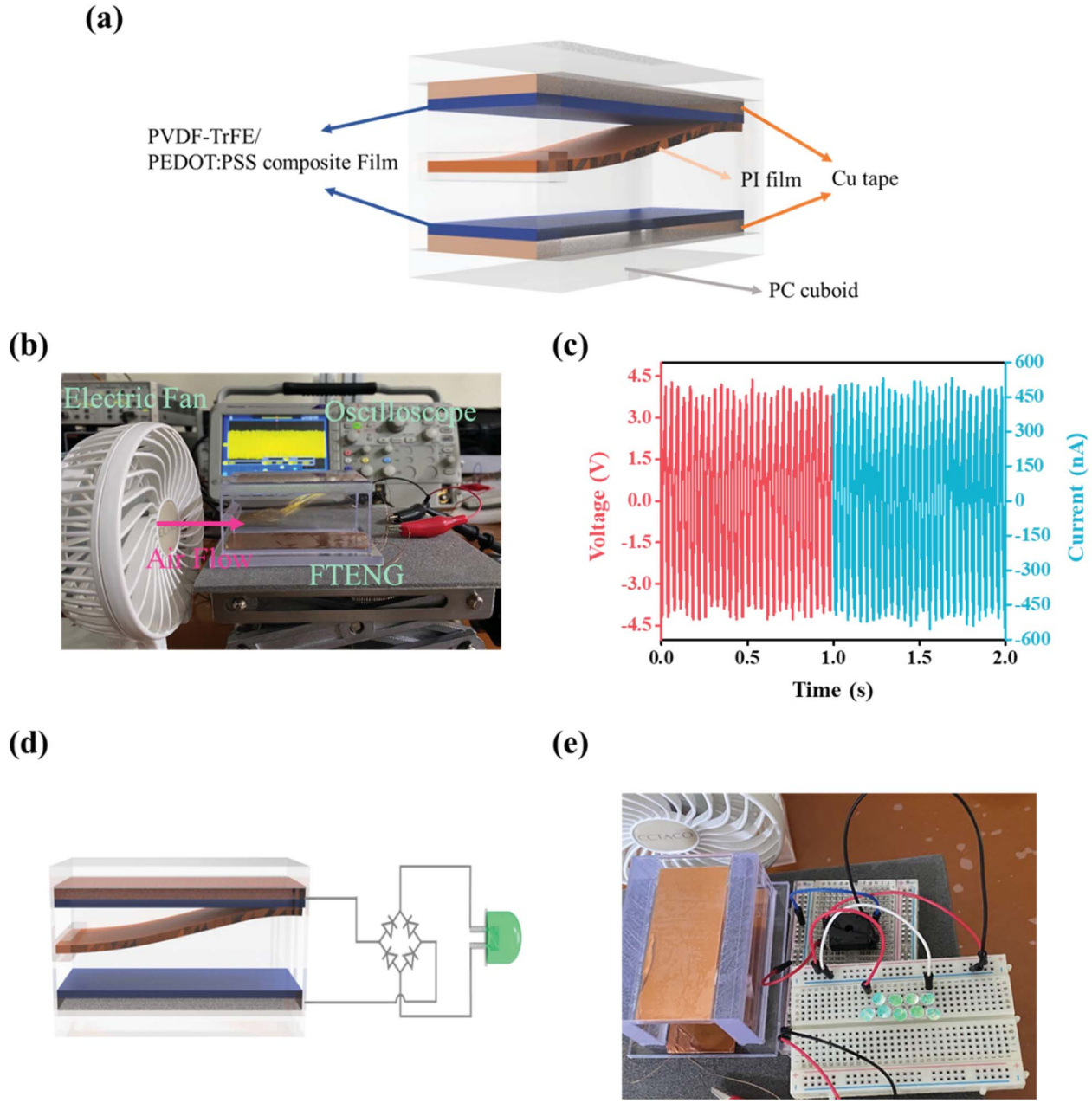

Fig. 7 (a) Schematic of flutter-driven TENG (FTENG). (b) FTENG acts according to flow. (c) The electrical output voltage and current of FTENG by electric fan. (d) Schematic illustration of the full-bridge circuit diagram. (e) Photograph of nine commercial green light-emitting diodes lit on by FTENG.

As shown in Fig. 5c, to estimate the external load resistance (R_L) on the electrical output performance of PVDF-TrFE/20 wt% PEDOT:PSS composite films, V_o and I_{sc} were measured at different R_L values from 80 kΩ to 960 MΩ. With the increase of R_L, the V_o value of PVDF-TrFE/20 wt% PEDOT:PSS composite films increased from 0.2 to 15.6 V, and the I_{sc} value decreased from 2.3 μA to 160 nA. In addition, the power density was 12.8 mW m^{-2} at an R_L of 2 MΩ (Fig. 5d). Compared with the power density of the PVDF-TrFE films, the maximum power density was shifted by 6 MΩ. These trends were observed at the other PEDOT:PSS contents (Fig. S4, Table S1†). It is thus shown that PEDOT:PSS has an effect on the internal resistance in PVDF-TrFE owing to its conductivity. The free mobile electrons in the conducting polymers have an effect on the movement of electrical charges in PVDF-TrFE.[28] Thus, it can be inferred that the composite films can generate more triboelectric charges. However, for contents above 20 wt% PEDOT:PSS, the power density decreased owing to the deterioration of the properties of the ferroelectric.

As the frequency of the PVDF-TrFE/20 wt% PEDOT:PSS composite films in the contact-separation mode varied from 1 Hz to 20 Hz (Fig. 6a and b), the corresponding V_o and I_{sc}

increased from 15 V to 68 V and from ~2 μA to ~23 μA, respectively. The V_o of the TENG should theoretically be constant at various frequencies. We used the wave driver to change the stroke distance between the PVDF-TrFE/PEDOT:PSS composite films and PI tapes with increasing frequency.[58] In addition, the capacitance changed and the charge accumulated on the composite films as the contact-separation frequencies increased; this increased the electrical output performance of the TENG.[59] The TENG using PVDF-TrFE/20 wt% PEDOT:PSS composite films was used to charge a capacitor from 1 to 1000 μF. The electrical output of the TENG was rectified by a full-bridge diode. The 1 μF capacitor which charged up to 3 V within 25 s (Fig. 6c). To utilize the wind energy, we demonstrated the FTENG. Fig. 7a schematically illustrates the FTENG. The FTENG is shown in Fig. 7b and Video S1.† The V_o and I_{sc} of FTENG using PVDF-TrFE/20 wt% PEDOT:PSS composite films generated 3.7 V and 450 nA, respectively, at an air flow rate of 6.5 m s^{-1} (Fig. 7c). The electrical output performance of FTENG using PVDF-TrFE films generated a V_o of 1.3 V and an I_{sc} of 210 nA (Fig. S5†). The FTENG was connected to a full-bridge rectifier, and nine commercial green LEDs which were connected in series instantly lit on *via* the FTENG (Fig. 7d, e and Video S2†). Additional studies in this area are needed to affect the wind velocity, size of the FTENG, and flutter materials.

The TENG performances of the PVDF-based composite films with nanofillers reported in the previous literatures are listed in Table S2.† The TENG performances would be a change in properties by the host materials with nanofillers or contacting the opposite materials. It can be seen that the PEDOT:PSS is effective nanofillers to enhance the triboelectric properties of PVDF-TrFE. Furthermore, it is expected that it will have the opportunity to be applied as a power supply for a variety of sensors.

4 Conclusions

In summary, we attempted to create all-organic triboelectric composite films with PVDF-TrFE and PEDOT:PSS. The PVDF-TrFE/PEDOT:PSS composite films maintained the characteristics of organic materials while they produced a high-electrical output. PEDOT:PSS was used as a nanofiller and was stably blended with PVDF-TrFE/PEDOT:PSS composite solutions. The effects of PEDOT:PSS at various weight ratios in PVDF-TrFE were investigated using XRD, FT-IR, and DSC. The XRD and FT-IR results showed that the electroactive phase of the composite films was preserved after the addition of different PEDOT:PSS concentrations in PVDF-TrFE. Additionally, the DSC analysis results showed an improvement X_c at different PEDOT:PSS concentrations compared with the PVDF-TrFE films. It seems that PEDOT:PSS affects the conformation of the ferroelectric characteristics. The electrical output performance reached a maximum at a PEDOT:PSS composite film content of 20 wt%, showing an open-circuit voltage of ~15 V, and a closed-circuit current of ~2.3 μA for oscillations at 1 Hz. The power density of the PVDF-TrFE/20 wt% PEDOT:PSS composite films was 12.8 mW m^{-2} at an R_L of 2 MΩ, which was shifted to an R_L of 6 MΩ for the PVDF-TrFE films. The dielectric constant value increased up to the PVDF-TrFE/30 wt% PEDOT:PSS composite films compared with the PVDF-TrFE films. It can be inferred that PEDOT:PSS has a leverage effect on the ferroelectric characteristics of PVDF-TrFE. Therefore, this led to an increase in the electrical output performance by improving the accumulation of triboelectric charges. These results indicate that PVDF-TrFE/20 wt% PEDOT:PSS composite films can be applied to FTENGs at a small-scale air flow. They have the potential as a power source for a variety of sensors.

Author contributions

Moon Hyun Chung: conceptualization, methodology, formal analysis, investigation, writing – original draft, writing – review & editing. Hyun-Jun Kim: methodology, formal analysis, writing – review & editing. Seunghwan Yoo: formal analysis, investigation, writing – review & editing. Hakgeun Jeong: supervision, investigation, validation, project administration, writing – review & editing. Kyung-Hwa Yoo: methodology, validation, supervision, writing – review & editing.

Conflicts of interest

The authors declare that they have no known competing financial interests or personal relationships that could have appeared to influence the work reported in this paper.

Acknowledgements

This research was supported by the Research and Development Program of the Korea Institute of Energy Research (Grant No. C1-2404). It was also supported by the Korea Institute of Energy Technology Evaluation and Planning (KETEP) grant funded by the Korea government (MOTIE) (20202020800030).

References

1 X. Cao, Y. Jie, N. Wang and Z. L. Wang, *Adv. Energy Mater.*, 2016, **6**, 1600665.
2 R. A. Whiter, C. Boughey, M. Smith and S. Kar-Narayan, *Energy Technol.*, 2018, **6**, 928–934.
3 G. Li, L. Li, P. Zhang, C. Chang, F. Xu and X. Pu, *RSC Adv.*, 2021, **11**, 17437–17444.
4 J. Chang, H. Meng, C. Li, J. Gao, S. Chen, Q. Hu, H. Li and L. Feng, *Adv. Mater. Technol.*, 2020, **5**, 1901087.
5 Z. Ren, Q. Zheng, H. Wang, H. Guo, L. Miao, J. Wan, C. Xu, S. Cheng and H. Zhang, *Nano Energy*, 2020, **67**, 104243.
6 X. Chen, Z. Ren, M. Han, J. Wan and H. Zhang, *Nano Energy*, 2020, **75**, 104980.
7 D. Kim, H. M. Lee and Y.-K. Choi, *RSC Adv.*, 2016, **7**, 137–144.
8 T. Quan and Y. Yang, *Nano Res.*, 2016, **9**(8), 2226–2233.
9 K. Zhang, S. Wang and Y. Yang, *Adv. Energy Mater.*, 2017, **7**, 1601852.
10 Y. Zhang, S.-C. Fu, K. C. Chan, D.-M. Shin and C. Y. H. Chao, *Nano Energy*, 2021, **88**, 106284.
11 X. Zhao, D. Zhang, S. Xu, W. Qian, W. Han and Y. Yang, *Adv. Mater. Technol.*, 2020, **5**, 2000466.

12 H. Ryu, J. H. Lee, T. Y. Kim, U. Khan, J. H. Lee, S. S. Kwak, H. J. Yoon and S. W. Kim, *Adv. Energy Mater.*, 2017, **7**, 1700289.
13 M. Kim, D. Park, M. M. Alam, S. Lee, P. Park and J. Nah, *ACS Nano*, 2019, **13**, 4640–4646.
14 J. P. Lee, J. W. Lee and J. M. Baik, *Micromachines*, 2018, **9**, 532.
15 K. Y. Lee, S. K. Kim, J. H. Lee, D. Seol, M. K. Gupta, Y. Kim and S. W. Kim, *Adv. Funct. Mater.*, 2016, **26**, 3067–3073.
16 L. Ruan, X. Yao, Y. Chang, L. Zhou, G. Qin and X. Zhang, *Polymers*, 2018, **10**, 1–27.
17 S. Cheon, H. Kang, H. Kim, Y. Son, J. Y. Lee, H. J. Shin, S. W. Kim and J. H. Cho, *Adv. Funct. Mater.*, 2018, **28**, 1703778.
18 Y. Park, Y. E. Shin, J. Park, Y. Lee, M. P. Kim, Y. R. Kim, S. Na, S. K. Ghosh and H. Ko, *ACS Nano*, 2020, **14**, 7101–7110.
19 S. Gupta, R. Bhunia, B. Fatma, D. Maurya, D. Singh, Prateek, R. Gupta, S. Priya, R. K. Gupta and A. Garg, *ACS Appl. Energy Mater.*, 2019, **2**, 6364–6374.
20 C. Ribeiro, C. M. Costa, D. M. Correia, J. Nunes-Pereira, J. Oliveira, P. Martins, R. Gonçalves, V. F. Cardoso and S. Lanceros-Méndez, *Nat. Protoc.*, 2018, **13**, 681–704.
21 P. Fakhri, H. Mahmood, B. Jaleh and A. Pegoretti, *Synth. Met.*, 2016, **220**, 653–660.
22 B. Wang and H. X. Huang, *Composites, Part A*, 2014, **66**, 16–24.
23 L. Wang, X. Yang and W. A. Daoud, *Nano Energy*, 2019, **55**, 433–440.
24 J. Chen, H. Guo, X. He, G. Liu, Y. Xi, H. Shi and C. Hu, *ACS Appl. Mater. Interfaces*, 2016, **8**, 736–744.
25 Y. Yu, Z. Li, Y. Wang, S. Gong and X. Wang, *Adv. Mater.*, 2015, **27**, 4938–4944.
26 X. Xia, J. Chen, H. Guo, G. Liu, D. Wei, Y. Xi, X. Wang and C. Hu, *Nano Res.*, 2017, **10**, 320–330.
27 M. Matsunaga, J. Hirotani, S. Kishimoto and Y. Ohno, *Nano Energy*, 2020, **67**, 104297.
28 S. Yu, Y. Zhang, Z. Yu, J. Zheng, Y. Wang and H. Zhou, *Nano Energy*, 2021, **80**, 105519.
29 V. A. Cao, S. Lee, M. Kim, M. M. Alam, P. Park and J. Nah, *Nano Energy*, 2020, **67**, 104300.
30 B. Zhang, G. Tian, D. Xiong, T. Yang, F. Chun, S. Zhong, Z. Lin, W. Li and W. Yang, *Research*, 2021, **2021**, 1–8.
31 H. Song, C. Liu, J. Xu, Q. Jiang and H. Shi, *RSC Adv.*, 2013, **3**, 22065–22071.
32 D. Ni, H. Song, Y. Chen and K. Cai, *Energy*, 2019, **170**, 53–61.
33 Z. Zhang, M. Liao, H. Lou, Y. Hu, X. Sun and H. Peng, *Adv. Mater.*, 2018, **30**, 1704261.
34 P. Talemi, M. Delaigue, P. Murphy and M. Fabretto, *ACS Appl. Mater. Interfaces*, 2015, **7**, 8465–8471.
35 S. Lee and Y. Lim, *Macromol. Mater. Eng.*, 2018, **303**, 1700588.
36 M. A. Khan, U. S. Bhansali and H. N. Alshareef, *Org. Electron.*, 2011, **12**, 2225–2229.
37 Y. Kim, J. Na, C. Park, H. Shin and E. Kim, *ACS Appl. Mater. Interfaces*, 2015, **7**, 16279–16286.
38 S. H. Jeong, S. Ahn and T. W. Lee, *Macromol. Res.*, 2019, **27**, 2–9.
39 G. Wang, H. Xia, X. C. Sun, C. Lv, S. X. Li, B. Han, Q. Guo, Q. Shi, Y. S. Wang and H. B. Sun, *Sens. Actuators, B*, 2018, **255**, 1415–1421.
40 A. Aliane, M. Benwadih, B. Bouthinon, R. Coppard, F. Domingues-Dos Santos and A. Daami, *Org. Electron.*, 2015, **25**, 92–98.
41 D. Mao, B. E. Gnade, M. A. Quevedo-Lopez, in *Ferroelectric Physical Effects*, ed. M. Lallart, IntechOpen, United Kingdom, 2011, vol. 4, pp. 77–100.
42 S. Chen, K. Yao, F. E. H. Tay and L. L. S. Chew, *J. Appl. Polym. Sci.*, 2010, **116**, 3331–3337.
43 S. Lanceros-Méndez, J. F. Mano, A. M. Costa and V. H. Schmidt, *J. Macromol. Sci., Part B: Phys.*, 2001, **40**, 517–527.
44 N. A. Shepelin, P. C. Sherrell, E. Goudeli, E. N. Skountzos, V. C. Lussini, G. W. Dicinoski, J. G. Shapter and A. V. Ellis, *Energy Environ. Sci.*, 2020, **13**, 868–883.
45 N. A. Shepelin, A. M. Glushenkov, V. C. Lussini, P. J. Fox, G. W. Dicinoski, J. G. Shapter and A. V. Ellis, *Energy Environ. Sci.*, 2019, **12**, 1143–1176.
46 X. Cai, T. Lei, D. Sun and L. Lin, *RSC Adv.*, 2017, **7**, 15382–15389.
47 S. Kulandaivalu, Z. Zainal and Y. Sulaiman, *Int. J. Polym. Sci.*, 2016, **2016**, 1–12.
48 P. Cebe and J. Runt, *Polymer*, 2004, **45**, 1923–1932.
49 T. Feng, D. Xie, Y. Zang, X. Wu, T. Ren and W. Pan, *Integr. Ferroelectr.*, 2013, **141**, 187–194.
50 J. Kim, J. H. Lee, H. Ryu, J. H. Lee, U. Khan, H. Kim, S. S. Kwak and S. W. Kim, *Adv. Funct. Mater.*, 2017, **27**, 1–8.
51 A. Lonjon, L. Laffont, P. Demont, E. Dantras and C. Lacabanne, *J. Phys. D: Appl. Phys.*, 2010, **43**, 345401.
52 G. S. Ekbote, M. Khalifa, A. Mahendran and S. Anandhan, *Soft Matter*, 2021, **17**, 2215–2222.
53 H. Zou, Y. Zhang, L. Guo, P. Wang, X. He, G. Dai, H. Zheng, C. Chen, A. C. Wang, C. Xu and Z. L. Wang, *Nat. Commun.*, 2019, **10**, 1427.
54 J. Kim, H. Ryu, J. H. Lee, U. Khan, S. S. Kwak, H. J. Yoon and S. W. Kim, *Adv. Energy Mater.*, 2020, **10**, 1903524.
55 S. Niu and Z. L. Wang, *Nano Energy*, 2014, **14**, 161–192.
56 W. Seung, H. J. Yoon, T. Y. Kim, H. Ryu, J. Kim, J. H. Lee, J. H. Lee, S. Kim, Y. K. Park, Y. J. Park and S. W. Kim, *Adv. Energy Mater.*, 2017, **7**, 1600988.
57 J. H. Lee, R. Hinchet, T. Y. Kim, H. Ryu, W. Seung, H. J. Yoon and S. W. Kim, *Adv. Mater.*, 2015, **27**, 5553–5558.
58 J. Wang, X. Li, Y. Zi, S. Wang, Z. Li, L. Zheng, F. Yi, S. Li and Z. L. Wang, *Adv. Mater.*, 2015, **27**, 4830–4836.
59 X. Xie, Y. Zhang, C. Chen, X. Chen, T. Yao, M. Peng, X. Chen, B. Nie, Z. Wen and X. Sun, *Nano Energy*, 2019, **65**, 103984.